

DEUTERIUM TOWARD THE WHITE DWARF WD 0621–376: RESULTS FROM THE *FAR ULTRAVIOLET SPECTROSCOPIC EXPLORER (FUSE)* MISSION

N. LEHNER,¹ C. GRY,^{2,3} K. R. SEMBACH,¹ G. HÉBRARD,⁴ P. CHAYER,^{1,5} H. W. MOOS,¹ J. C. HOWK,¹ AND J.-M. DÉSSERT⁴

Version of November 6, 2018

ABSTRACT

Far Ultraviolet Spectroscopic Explorer observations are presented for WD 0621–376, a DA white dwarf star in the local interstellar medium (LISM) at a distance of about 78 pc. The data have a signal-to-noise ratio of ~ 20 –40 per 20 km s^{−1} resolution element and cover the wavelength range 905–1187 Å. LISM absorption is detected in the lines of D I, C II, C II*, C III, N I, N II, N III, O I, Ar I, and Fe II. This sight line is partially ionized, with an ionized nitrogen fraction of > 0.23 . We determine the ratio $D/O = (3.9 \pm 1.3) \times 10^{-2}$ (2σ). Assuming a standard interstellar oxygen abundance, we derive $D/H \approx 1.3 \times 10^{-5}$. Using the value of $N(\text{H I})$ derived from *EUVE* data gives a similar D/H ratio. The D I/N I ratio is $(3.3 \pm 0.8) \times 10^{-1}$ (2σ).

Subject headings: ISM: abundances – ultraviolet: ISM – ISM: structure – white dwarfs – stars: individual: WD 0621–376

1. INTRODUCTION

Deuterium measurements place fundamental constraints on Big Bang nucleosynthesis (BBN), the amount of baryons in the Universe, and the chemical evolution of galaxies (see Tytler et al. 2000). Deuterium is thought to be formed by primordial BBN, and has subsequently been processed in stellar interiors. Therefore, the abundance of D should decrease with time and local D/H measurements should provide lower limits to the primordial D abundance. By comparing local measurements with measurements obtained for distant intergalactic clouds toward quasars, a better picture of the chemical evolution of the galaxies can be drawn. A key step is to establish a robust set of measurements for environments within the Galaxy. This has not yet been done, and the picture that now exists is complicated by several recent studies. Linsky (1998) obtained a nearly constant ratio of $D/H = (1.5 \pm 0.1) \times 10^{-5}$ in the Local Interstellar Cloud (LIC), while other investigations (Laurent et al. 1979; York 1983; Vidal-Madjar et al. 1998; Hébrard et al. 1999; Jenkins et al. 1999; Sonneborn et al. 2000) suggest variations amongst the different sight lines probing gas beyond the LIC. Possible causes of D/H variations are numerous (Lemoine et al. 1999), but none have yet been definitely implicated in causing the observed variations.

The *Far Ultraviolet Spectroscopic Explorer (FUSE)* is capable of directly observing deuterium absorption in the Lyman series lines (except Lyman- α) at ultraviolet (UV) wavelengths shortward of 1200 Å. Access to higher order Lyman lines allows a larger variety of environments (more distant, denser clouds) to be observed than is possible with the *Hubble Space Telescope* or IMAPS. Therefore, *FUSE* measurements are essential for a better description of the

possible D/H variations that may occur within the interstellar medium (ISM) of the Galaxy.

We present the first measurement of deuterium absorption toward the white dwarf WD 0621–376 ($l, b = 245.41^\circ, -21.43^\circ$; $V = 12.0$). The star is a hot ($T_{\text{eff}} \approx 62,000$ K), metal-rich DA white dwarf (Holberg et al. 1993) with a smooth stellar continuum. It lies at a photometric distance of $\simeq 78$ pc (Holberg et al. 1998). In agreement with the *IUE* observations, no He II absorption (e.g., $\lambda\lambda 992.3, 1084.9$) is seen in the *FUSE* spectrum; therefore continuum placement for the observed D I lines in the *FUSE* band is not affected adversely by the far-UV He II series.

This article is part of a series dedicated to the first *FUSE* measurements of deuterium along sight lines toward Feige 110 (Friedman et al. 2001), WD 2211–495 (Hébrard et al. 2001), HZ 43A (Kruk et al. 2001), G 191–B 2B (Lemoine et al. 2001), BD +28° 4211 (Sonneborn et al. 2001), and WD 1634–573 (Wood et al. 2001). Moos et al. (2001) present a synthesis of these results.

2. FUSE OBSERVATIONS AND DATA PROCESSING

FUSE is a dedicated observatory providing access to the 905–1187 Å wavelength range at high spectral resolution. The design and performance of the *FUSE* spectrograph have been described by Moos et al. (2000) and Sahnou et al. (2000), respectively. Two sets of *FUSE* observations of WD 0621–376 were obtained in histogram accumulation mode: On December 6, 2000, 19 exposures totaling an exposure time of 8.3 ks were obtained through the large $30'' \times 30''$ aperture (LWRS), while on February 3, 2001, 21 exposures totaling 9.8 ks were obtained with the medium $4'' \times 20''$ aperture (MDRS). The data are archived

¹ Department of Physics and Astronomy, The Johns Hopkins University, Bloomberg Center, 3400 N. Charles Street, Baltimore, MD 21218. nl@pha.jhu.edu

² ISO Data Center, ESA, Astrophysics Division, P.O. Box 50727, 28080 Madrid, Spain.

³ Laboratoire d'Astronomie Spatiale, B.P. 8, F-13376 Marseille, France.

⁴ Institut d'Astrophysique de Paris, 98^{bis} boulevard Arago, F-75014 Paris, France.

⁵ Department of Physics and Astronomy, University of Victoria, P.O. Box 3055, Victoria, BC V8W 3P6, Canada.

in the Multi-Mission Archive at the Space Telescope Institute under the observation identifications P1041501 and P1041502. To reduce the effects of detector fixed-pattern noise, the data were acquired using focal plane split motions, wherein subsequent exposures are placed at different locations on the detector. Unfortunately, at the time of the observations this mode was not fully operational and caused misalignments of different channels during some exposures. For the LWRS observations, 8 exposures were lost in the SiC2 channels. For the MDRS observations, only the LiF1 channels were properly aligned; for LiF2, 9 exposures were lost (for 7 exposures the detector was off); for SiC1, 6 exposures were lost; and for SiC2 only two exposures were aligned. Airglow emission lines were reduced along with the stellar spectra, but their intensities were minimized as most of exposures were obtained during orbital night (except for two exposures for each observation).

Standard processing with the current version of the calibration pipeline software (CALFUSE v1.8.7) was used to extract and calibrate the spectra. This version of the pipeline does not yet correct for the astigmatism or flat-field, and therefore we required any absorption features to be present in at least two channels to be considered real. The extracted spectra associated with the separate exposures of a given observation were aligned by cross-correlating the positions of strong interstellar lines, co-added, and rebinned to a nominal spectral resolution of $\sim 15,000$ ($\approx 20 \text{ km s}^{-1}$). The interstellar lines were shifted to 0 km s^{-1} in the laboratory rest frame (note, however, that *IUE* spectra gave a heliocentric velocity of $40.5 \pm 0.5 \text{ km s}^{-1}$, Holberg et al. 1998). Including or removing the two daylight exposures in each observation did not change the strengths of the airglow lines, and therefore all the exposures were co-added to maximize the signal-to-noise levels (S/N). To maintain an optimal spectral resolution and information on the fixed-pattern noise, neither the individual segments, nor the LWRS and MDRS observations were co-added together.

We present reduced spectra for several different detector segments in Figure 1. The data reveal numerous stellar and interstellar absorption lines. Prominent interstellar lines are identified.

3. ANALYSIS

We used two different methods to derive the column densities of the interstellar species observed toward WD0621–376: (1) The apparent optical depth method (AOD, Savage and Sembach 1991) was used to derive column densities and to check for unresolved saturated structures within the observed profiles. A direct integration of the apparent column density profiles, $N_a(v) = 3.768 \times 10^{14} \tau_a(v) / [f\lambda(\text{\AA})]$, over the velocity range yields the true total column density in cases where the absorption is weak ($\tau \lesssim 1$) or the lines are resolved. Equivalent widths were directly measured by integrating the observed intensity. (2) A profile fitting (PF) method using the code Owens was also used to obtain the column densities of D I, N I, O I, and Fe II. The reader should refer to Hébrard et al. (2001) for a full description of the PF method, and we will concentrate on describing in details the AOD results. The two approaches are different and

complementary. Some of the issues involved in using these two methods are discussed by Jenkins (1996). By using both approaches, we have a consistency check on the derived column densities and systematic errors associated with the measurements of each particular method. All methods are subject to a systematic uncertainty due to the possible presence of a broad component in the instrumental line spread function (LSF). Several tests (Wood et al. 2001; Hébrard et al. 2001; Kruk et al. 2001) show however that the uncertainty due to this effect is negligible for weak metal lines of the type discussed in this paper. Consequently, for the profile fitting method, the LSF was modeled with a single gaussian component. Examples of how the LSF handling in the profile fitting affects the column density results are discussed in § 3.2.

We adopted wavelengths and oscillator strengths from the Morton (2000, private communication) atomic data compilation. This compilation is similar to the Morton (1991) compilation with a few minor updates to the atomic parameters for lines of interest in this study.

3.1. Apparent optical depth method

3.1.1. Interstellar absorption

The stellar continuum was simple enough near the C II, C II*, C III, N I, N II, N III, O I, Ar I, and Fe II features to be fitted with low-order (≤ 3) Legendre polynomials. Equivalent widths and apparent column densities are summarized in Table 1, where lower limits indicate that the line contains some unresolved, saturated absorption that cannot be reliably estimated with the existing data. Comparisons of the data from multiple channels were used to check for fixed-pattern noise and systematic continuum placement problems. For the measurements the following segments were used: SiC1B (905–992 Å); SiC2A (917–1005 Å); SiC1A (1003–1091 Å); LiF1A (987–1082 Å); LiF1B (1094–1187 Å); LiF2A (1087–1182 Å). The last column in Table 1 indicates which segments were used to study each line. In this column, the absence of a segment indicates that there may be a detector defect at this wavelength (e.g., SiC2A has more bad pixels than SiC1B, especially in the range 960–965 Å near the N I lines). Although the measurements were cross-checked and were in agreement in the different segments indicated in Table 1, we adopted the values of equivalent width and apparent column density from the segments having the best quality data. Exceptions are the SiC2A LWRS and SiC1B LWRS and MDRS channels that have comparable quality data; the values for lines measured on these segments were averaged (all the measured values were within the estimated 1σ errors of the individual measurements).

To check if the lines contain some unresolved saturated structure, the apparent column density profiles of two or more lines of a given species with different values of $f\lambda$ were directly compared (N I and O I). The N I transitions at 963.99 and 965.05 Å are affected by an unknown source of noise, and this results in a column density that cannot be reconciled with the values derived from other lines (see Table 1). This discrepancy is unlikely to arise from the adopted oscillator strengths, as studies of other sight lines do not show any particular problem for these transitions. Since we have information from different channels (see last column in Table 1), fixed-pattern noise also seems

unlikely. Contamination by unidentified photospheric stellar lines is the most likely source of confusion since this star is metal rich. These two lines were removed from the analysis. Of the remaining N I lines, only N I $\lambda 1134.98$ suffers from weak saturation effects. Similar comparisons were made for O I, and the transitions at 948.686, 971.738 and 1039.230 Å contain unresolved saturated structures (see Table 1). We note that, while the total column densities of all the unsaturated lines of N I and O I agree remarkably well within the 1σ errors, the strongest N I $\lambda\lambda 953.655$, 1134.415 and O I $\lambda\lambda 936.630$, 976.448 lines yield the lowest apparent column densities, indicating some weak saturation effects might be present. For the other species, assuming they follow a similar curve of growth, only C II and N II are likely to be influenced strongly by saturation effects.

Both C III and N III are blended with their respective stellar features. Figure 2 shows a stellar model ($T_{\text{eff}} = 62,000$ K; $\log g = 7.0$, $\log C/H = -6.0$; $\log N/H = -6.6$, preliminary results from Chayer et al., in preparation) that estimates the stellar contribution ($\sim 30\%$ for C III, $\sim 7\%$ for N III). The stellar model was aligned to the observed stellar lines, and an offset of $\approx +14 \text{ km s}^{-1}$ was found with respect to the interstellar lines. N III suffers from blending with interstellar Si II $\lambda 989.87$ absorption, which is clearly visible in Figure 2, but the combination of relatively low spectral resolution and the proximity of the N III stellar feature did not allow us to model this line. We examined the *IUE* spectrum of WD 0621–376 to check for Si II absorption at longer wavelengths, but its poor quality did not shed any light on the amount of Si II along this sight line. Therefore, the derived equivalent width of N III must be considered an upper limit.

The spectra also show the detection of a very weak feature Fe II at 1144.938 Å. Though its measurement remains uncertain, its identification is unambiguous as the radial velocity of this feature is in agreement with the velocities of the N I lines in the LiF 1B and LiF 2A segments.

The 3σ upper limits for the equivalent widths in Table 1 are defined as $W_{\text{min}} = 3\sigma \delta\lambda$, where σ is the inverse of continuum S/N ratio and $\delta\lambda \approx 0.1$ Å, which is approximately the average FWHM obtained from the resolved features. The corresponding 3σ upper limits on the column density are obtained from the corresponding equivalent width limits and the assumption of a linear curve of growth.

3.1.2. Deuterium absorption

D I Lyman- β is well detected in the *FUSE* spectra of WD 0621–376 (see Figure 3). Figure 4 shows some evidence for tentative detections of D I $\lambda 972$ and D I $\lambda 949$. Polynomial fits to the continua are shown for different segments along with their respective normalized profiles with optimized gaussian fits (see below). Except for segment SiC 2A, all the measurements for D I $\lambda\lambda 972$ and 949 yield detections with less than 3σ significance (see Table 2). For segment SiC 2A, both the continuum placement and the line detection remain very uncertain and fixed-pattern noise may contaminate this feature. The measurements of these lines and the 3σ upper limits on W_λ and $\log N$ were derived following the same methods described in § 3.1.1.

Figure 3 displays the D I Lyman- β spectra in the different segments. We note that the H I airglow is relatively

strong and broad ($\sim 100 \text{ km s}^{-1}$) in the LWRs data. Its strength varies in the different segments; for these data, the airglow in segments LiF 2B and SiC 1A affects the D I measurement. The MDRS observations are less affected by the airglow, but it is clearly present. The LiF 2B D I data are more affected by the H I airglow than the LiF 1A data.

The measurements for D I are summarized in Table 2. The continuum placement is more complicated than for the species described in § 3.1.1, requiring higher order (3–5) polynomial fits to the continuum. The continuum fits in the LWRs LiF 2B and SiC 1A segments are very uncertain due to the airglow contamination; the measurements, however, agree with the other measurements (Table 2). Generally good agreement is found between the MDRS LiF 1A, LiF 2B and LWRs LiF 1A data. Of these, the MDRS LiF 1A is the least affected by airglow, so we adopt this result ($\log N(\text{D I}) = 13.75 \pm 0.09 \text{ dex}$, 1σ) for comparison with the other value derived below.

The continuum was also determined using the stellar model described in § 3.1.1 for the MDRS LiF 1A observations: The top panel of Figure 5 shows the model overplotted on the data. While Figure 5 shows a reasonable stellar model, there are still some problems as some portions of the spectrum are not so well reproduced by the stellar model. To estimate the contribution from the H I feature, the normalized profile (bottom panel of Figure 5) was fitted with 3 gaussian absorption components using an optimized routine (Howarth et al. 1996), where the FWHM and the centroids were free to vary; changing (in a reasonable manner) the initial guess of these parameters did not change the fit. This method does not attempt to produce any realistic physical quantities for H I, but just tests the effective continuum placement for D I, as optimized gaussian fits can usually reproduce complicated profiles (Lehner et al. 1999). The bottom panel of Figure 5 also shows the same fit with 2 gaussian components to the H I feature (FWHMs and centroids were fixed to the values derived with the 3 components fit) to indicate the degree of contamination from H I to D I. This approach yields a logarithmic apparent column density of $13.84 \pm 0.10 \text{ dex}$ (1σ). Considering other segments gives similar results, but these are more uncertain as the airglow is stronger.

The above estimates of $N(\text{D I})$ agree within their 1σ errors, though the difference in the absolute values shows some uncertainties caused by the continuum placement. We adopt $\log N(\text{D I}) = 13.79 \pm 0.14 \text{ dex}$ (2σ), obtained by doing a weighted mean of the apparent column densities derived using the two different continuum placements. Table 3 summarizes the definitive results for the different ions (for N I and O I, the values are weighted means of the values listed in Table 1).

As discussed above, the S/N levels for the higher D I Lyman series were not high enough to make precise estimates of $N(\text{D I})$. However, their 3σ upper limits do not suggest that the D I Lyman- β line is strongly saturated, if at all. Comparing the apparent optical depths of D I Lyman- β with the unsaturated N I and O I lines (see Figure 6) indicates that the D I Lyman- β optical depths for the two continuum placements are only as strong as the strongest N I and O I features, suggesting that the line might not be entirely resolved (see § 3.1.1). However, sat-

uration corrections should be small ($\lesssim 0.05$ dex according to the N I and O I lines) and are less than the 2σ error bars on the measurement.

3.2. Results of the profile fitting and comparison

In addition to estimating column densities using the apparent optical depth method, two independent profile fitting analyses using voigt profiles and using the information simultaneously from all the windows were performed, leading to two sets of results, PF 1 and PF 2. In PF 1, the profile fitting code Owens was used to fit the data in 32 spectral windows, including all available unsaturated lines from D I, N I, O I and Fe II (i.e., N I $\lambda 1134.980$, O I $\lambda\lambda 948.686, 971.738$ and 1039.230 were excluded). In PF 2, a total of 24 windows were used including lines from D I, N I, and O I. For Lyman- β , only the MDRS data were used in both cases because the LWRs data are significantly affected by airglow. The results for these two methods are listed in Table 3. Although there are differences both in the absolute values and in the estimated 2σ errors, all results agree within 1σ . Apart from the different number of windows used, the differences in the results arise from the strategies adopted to deal with the widths of the LSF. The LSFs are not yet well characterized and are known to vary from one segment to another. In PF 1 the LSF widths of about 60% of the windows were fixed to a pre-defined value (ranging from 8.7 to 12 pixels, depending on the window), while in PF 2 the LSF widths were free to vary, with the constraint that they remain within plausible values (in the accepted fits the maximum FWHM was 15 pixels and the minimum was 6 pixels).⁶

The largest differences, found for the N I column densities, are due to the fact that in PF 2 high column density values – implying saturation of some of the fitted N I lines – were permitted by the adoption of broader LSFs.

The top and middle panels of Figure 7 show the best fits to the D I Lyman- β line in the LiF 1A MDRS channel, as obtained by PF 1 ($\log N(\text{D I}) = 13.89$ dex) and PF 2 ($\log N(\text{D I}) = 13.86$ dex), respectively. As expected, there is no difference in the fitted profiles, but the difference in the adopted fit parameters can be seen in the profiles plotted before convolution with the LSF. The unconvolved profile is slightly narrower (and deeper) in PF 1 than in PF 2 because of a slightly lower b -value (7.1 vs 8.9 km s⁻¹) required to compensate for a slightly higher LSF width (10.5 vs 9.4 pixels in the LiF 1A MDRS data).

The bottom panel of Figure 7 shows a fit performed with Owens using the PF 2 method but fixing the D I column density to the best value ($\log N(\text{D I}) = 13.79$ dex) derived in § 3.1.2 using the AOD method. In this case, the unconvolved profile is shallower than the other two, but the convolved profile is not, because this is compensated by a narrow LSF (8 pixels). For the AOD value the optical depth of the Lyman- β line is smaller than 1. For the two best fits in PF 1 and PF 2, the Lyman- β line is slightly saturated, explaining why the D I column density results obtained by the two profile fitting studies are higher than those obtained by the AOD method.

The results obtained by the three independent investi-

gations are shown in Table 3. They all agree within the estimated 1σ errors. Our adopted result, shown in the last column of Table 3, is the simple mean between these three results.

4. NEUTRAL AND PARTIALLY IONIZED GAS

O I is an excellent tracer of neutral gas as its ionization potential and charge exchange reactions with hydrogen ensure that the ionization of H I and O I are strongly coupled. $N(\text{O I})/N(\text{H I})$ is therefore an excellent approximation of the ratio O/H. (Similarly the ratio D/O is well approximated by $N(\text{D I})/N(\text{O I})$). Therefore, using the Meyer et al. (1998) interstellar O abundance⁷, $\text{O}/\text{H} = (3.43 \pm 0.15) \times 10^{-4}$, and the O I column density along the WD 0621–376 sight line, we derive a total H I column density of 18.73 dex. We note, however, that the Meyer et al. sight lines typically sample more distant (100–1000 pc) gas than the WD 0621–376 sight line. From the *FUSE* spectra, it is not possible to derive a reliable H I column density, as the H I transitions are essentially confined on the flat part of the curve of growth for this sight line. Previously, Holberg et al. (1998) quoted $\log N(\text{H I}) = 18.15 \pm 0.15$ dex (1σ), which is not in agreement with our value derived above. Using *EUVE* spectra, Wolff et al. (1998) found 18.70 dex, in good agreement with the value derived from O I, but unfortunately no error is quoted. Considering the *IUE* spectrum, we note that it is not possible to obtain H I from these data due to its relatively low quality. Only a combination of a very high S/N spectrum and a very good stellar model would help to directly determine the H I column density to a reasonable degree of accuracy.

With the derived N I column density and the Meyer et al. (1997) interstellar N abundance, $N/\text{H} = (7.5 \pm 0.4) \times 10^{-5}$, one finds 18.47 dex for H I, a value of about 48% lower than the value derived from O I. The *FUSE* bandpass allows us to directly estimate the quantity of ionized nitrogen, as N II and N III are accessible. N III is too poorly determined to be of much use as the amount of Si II remains unknown. However, the ratio $N \text{ I}/(N \text{ I} + N \text{ II}) < 0.77$ again suggests that a substantial fraction ($>23\%$) of N is ionized. Therefore, the discrepancy in values of $N(\text{H I})$ derived from N I and O I may be due in part to ionization of N in H I gas along the sight line. While the charge exchange with hydrogen should make N I a good indicator of the amount of H I along the sight line (Sofia and Jenkins 1998), Jenkins et al. (2000) noted that in regions where $n_e \gg n_{\text{H}^0}$, N may show a deficiency of its neutral form, similar to what is observed for argon.

A similar result holds for the ionization of argon. Using our derived Ar I column density and the Ar abundance from Anders and Grevesse (1989), $\text{Ar}/\text{H} = (3.6 \pm_{0.7}^{0.9}) \times 10^{-6}$, we derive an H I column density of about 18.30 dex, which, when compared to the value derived from O I, implies that 65% of the argon is ionized (neither Ar nor N is depleted significantly onto dust grains). These results for both N I and Ar I indicate that photoionization may be an important process along this sight line. Towards four other nearby white dwarfs Jenkins et al. (2000), similar results

⁶ Note that the dispersions of the *FUSE* spectrographs are ~ 6.7 and ~ 6.2 mÅ per pixel for LiF and SiC channels, respectively.

⁷ Meyer et al.'s value ($\text{O}/\text{H} = (3.19 \pm 0.14) \times 10^{-4}$) was corrected for the recommended oscillator strength of O I $\lambda 1356$ ($f = 1.16 \times 10^{-6}$ instead of $f = 1.25 \times 10^{-6}$) by Welty et al. (1999).

were found, favoring the idea that the LISM ionization is maintained by a strong extreme ultraviolet flux (yet to be identified) rather than an incomplete recombination of helium from a previous episode of collisional ionization at high temperatures. The presence of C III also implies that the gas is partially ionized. Fe II is largely deficient (-1.3 dex), but this is at least partly explained by iron being depleted onto dust grains.

5. D/O, D/N AND D/H RATIOS

Using the results from Table 3, and following the above discussion ($D/O = D\text{ I}/O\text{ I}$), we calculate $D/O = (3.9 \pm 1.3) \times 10^{-2}$ (2σ). Using the interstellar O abundance, the D/H ratio can be derived: $D/H \approx 1.3 \times 10^{-5}$. A similar D/H ratio ($D/H \sim 1.4 \times 10^{-5}$) is obtained using $N(\text{H I})$ derived from the *EUVE* spectra.

The D I/N I ratio is $(3.3 \pm 1.0) \times 10^{-1}$ (2σ). As there is a non negligible fraction of ionized nitrogen and some of this fraction can be either in H I or H II regions, it is not possible to derive the ratio D/H using the nitrogen abundance.

Toward WD 0621–376, the H I column density remains relatively uncertain, but D/H is consistent with the LIC ratio ($(1.5 \pm 0.1) \times 10^{-5}$, Linsky 1998) and also consistent with other measurements within the LISM (Moos et al. 2001). Since in the *FUSE* bandpass, D I and O I can be generally measured simultaneously, D/O ratio (more precisely measured) can be used instead of D/H. To be noted that if D/O becomes available in distant quasars, the D/O ratio would be very sensitive to astration since D I is destroyed while O I is enhanced through the various stellar cycles. Initial measurements of D/O ratios in the LISM (Moos et al. 2001) show no significant variations which also

favors constant D/H and O/H ratios in the LISM. Other results suggest variations at larger distances (e.g., Jenkins et al. 1999; Sonneborn et al. 2000), but more observations beyond the LISM wall are needed to have a better understanding of these possible variations in the ISM.

6. SUMMARY

We have presented *FUSE* observations of the DA white-dwarf star WD 0621–376, located at about 78 pc. The spectra show interstellar absorption from D I, C II, C II*, C III, N I, N II, N III, O I, Ar I, and Fe II. Using both the N ISM abundance and the N I and N II column densities, we showed that N is ionized by a fraction $>23\%$ (Ar is ionized by about 65%). These results confirm the recent suggestion by Jenkins et al. (2000) that a diffuse ionizing flux (> 24.6 eV) creates the high fraction of ionized helium observed in the LISM.

The D/O ratio along the WD 0621–376 sight line is $(3.9 \pm 1.3) \times 10^{-2}$ (2σ), implying a D/H ratio of approximately 1.3×10^{-5} . This D/H ratio is also supported by the H I measurement obtained from *EUVE*. The D I/N I ratio is $(3.3 \pm 1.0) \times 10^{-1}$ (2σ). Both D/O and D/H ratios are in agreement with other LISM measurements, implying that D/O and D/H are relatively homogeneous in the LISM.

This work is based on data obtained for the Guaranteed Time Team by the NASA-CNES-CSA *FUSE* mission operated by the Johns Hopkins University. Financial support to U. S. participants has been provided by NASA contract NAS5-32985. French participants are supported by CNES. This work was partially done using the profile fitting procedure Owens.f developed by M. Lemoine and the *FUSE* French Team.

REFERENCES

- Anders, E., Grevesse, N., 1989, *Geochim. Cosmochim. Acta*, 53, 197
 Finley, D. S., Koester, D., Basri, G. 1997, *ApJ*, 488, 375
 Friedman, S. D., et al. 2001, *ApJS*, submitted
 Hébrard, G., Mallouris, C., Ferlet, R., Koester, D., Lemoine, M., Vidal-Madjar, A., York, D. G. 1999, *A&A*, 350, 643
 Hébrard, G., et al. 2001, *ApJS*, submitted
 Howarth, I. D., Murray, J., Mills, D., Berry, D. S. 1996, *STARLINK User Note SUN 50*, Rutherford Appleton Laboratory/CCLRC
 Holberg, J. B., et al. 1993, *ApJ*, 416, 806
 Holberg, J. B., Barstow, M. A., Sion, E. M. 1998, *ApJS*, 119, 207
 Jenkins, E. B. 1996, *ApJ*, 471, 292
 Jenkins, E. B., et al. 2000, *ApJ*, 538, L81
 Jenkins, E. B., Tripp, T. M., Woźniak, P. R., Sofia, U. J., Sonneborn, G. 1999, *ApJ*, 520, 182
 Kruk, J. W., et al. 2001, *ApJS*, submitted
 Laurent, C., Vidal-Madjar, A., York, D. G. 1979, *ApJ*, 229, 923
 Lehner, N., Sembach, K. R., Lambert, D. L., Ryans, R. S. I., Keenan, F. P., 1999, *A&A*, 352, 257
 Lemoine, M., et al. 1999, *New Astronomy*, 4, 231
 Lemoine, M., et al. 2001, *ApJS*, submitted
 Linsky, J. L. 1998, *Space Sci. Rev.*, 84, 285
 Meyer, D. M., Jura, M., Cardelli, J. A. 1998, *ApJ*, 493, 222
 Meyer, D. M., Cardelli, J. A., Sofia, U. J. 1997, *ApJ*, 490, L103
 Moos, H. W., et al. 2000, *ApJ*, 538, L1
 Moos, H. W., et al. 2001, *ApJS*, submitted
 Morton, D. C. 1991, *ApJS*, 77, 119
 Savage, B. D., Sembach, K. R. 1991, *ApJ*, 379, 245
 Sahnou, D. J., et al. 2000, *ApJ*, 538, L7
 Sofia, U. J., Jenkins, E. B. 1998, *ApJ*, 499, 951
 Sonneborn, G., Tripp, T. M., Ferlet, R., Jenkins, E. B., Sofia, U. J., Vidal-Madjar, A., Woźniak, P. R. 2000, *ApJ*, 545, 277
 Sonneborn, G., et al. 2001, *ApJS*, submitted
 Tytler, D., O'Meara, J. M., Suzuki, N., Lubin, D. 2000, *Phys. Rep.*, 333, 409
 Vidal-Madjar, A., et al. 1998 *A&A*, 338, 694
 Welty, D. E., Hobbs, L. M., Lauroesch, J. T., Morton, D. C., Spitzer, L., York, D. G. 1999, *ApJS*, 124, 465
 Wolff, B., Koester, D., Dreizler, S., Haas, S. 1998, *A&A*, 329, 1045
 Wood, B. E., et al. 2001, *ApJS*, submitted
 York, D. G. 1983, *ApJ*, 264, 172

TABLE 1
INTERSTELLAR ABSORPTION LINES (BUT D I): EQUIVALENT WIDTHS AND AOD RESULTS

Ions	λ_{lab}^a Å	f^a	S/N ^b	W_λ (mÅ)	$\log N_a$ (cm ⁻²)	Segment ^b
C II	1036.337	1.18×10^{-1}	33	98.9 ± 2.5	> 14.19	1,(2,3)
C II*	1037.018	1.25×10^{-1}	54	12.8 ± 1.5	13.06 ± 0.05	1,(2,3)
C III	977.020	7.62×10^{-1}	24	62.5 : ^c	> 13.14 : ^c	4,5
N I	953.415	1.32×10^{-2}	32	21.5 ± 3.0	14.34 ± 0.07	4,6
	953.655	2.50×10^{-2}	30	32.9 ± 5.0	14.29 ± 0.07	4,5,6
	953.970	3.48×10^{-2}	30	41.2 : ^d	14.24 : ^d	4,5,6
	963.990	1.48×10^{-2}	37	30.8 ± 2.3	14.47 ± 0.04	6,(4)
	964.626	9.43×10^{-3}	30	16.4 ± 2.9	14.35 ± 0.08	5,6
	965.041	4.02×10^{-3}	32	16.0 ± 3.3	14.72 ± 0.15	5,6
	1134.165	1.52×10^{-2}	48	34.1 ± 3.1	14.35 ± 0.04	8,(7)
	1134.415	2.97×10^{-2}	35	51.6 ± 2.8	14.31 ± 0.04	8,(7)
	1134.980	4.35×10^{-2}	44	56.2 ± 2.8	> 14.18	8,(7)
N II	915.613	1.65×10^{-1}	20	51.5 :	> 13.74 :	5,6
	1083.994	1.15×10^{-1}	40	58.2 ± 2.8	> 13.80	3,(9)
N III	989.799	1.23×10^{-1}	21	< 79.0 : ^e	< 13.94 : ^e	1,(2,3)
O I	924.950	1.54×10^{-3}	26	17.8 ± 3.9	15.23 ± 0.08	5,6,(4)
	929.517	2.29×10^{-3}	25	21.8 ± 3.9	15.22 ± 0.08	4,5,6
	936.630	3.65×10^{-3}	26	37.1 ± 4.5	15.20 ± 0.10	4,5,6
	948.686	6.31×10^{-3}	23	57.1 ± 4.4	> 15.13	4,5,6
	950.885	1.58×10^{-3}	21	18.8 ± 4.3	15.22 ± 0.09	4,(5,6)
	971.738	1.16×10^{-2}	23	69.6 ± 4.7	> 15.04	4,5,6
	976.448	3.31×10^{-3}	23	34.2 ± 6.8	15.17 ± 0.15	4,5,6
	988.773	4.65×10^{-2}	25	... ^f	... ^f	4,(5,6)
	1039.230	9.20×10^{-3}	32	79.6 ± 3.4	> 15.11	1,(2,3)
Si II	989.873	1.87×10^{-1}	26	... ^e	... ^e	1,(2,3)
	1020.699	1.64×10^{-2}	41	< 7.3	< 13.68	1,(2,3)
Ar I	1048.220	2.63×10^{-1}	41	17.6 ± 2.8	12.86 ± 0.07	1,(2,3)
	1066.660	6.65×10^{-2}	40	... ^g	... ^g	1
Fe II	1144.938	1.06×10^{-1}	42	7.3 ± 2.5	12.88 ± 0.15	7,8

Note. — Uncertainties are 1σ error. Upper limits indicate that no feature is present and are 3σ estimates, except for N III. Lower limits indicate that the absorption line is saturated. Colons indicate that the value is uncertain. (See text for more details).

(a) Rest frame vacuum wavelengths and oscillator strengths are from Morton (private communication, 2000).

(b) 1: LiF 1A MDRS; 2: LiF 1A LWRS; 3: SiC 1A LWRS; 4: SiC 2A LWRS; 5: SiC 1B MDRS; 6: SiC 1B LWRS; 7: LiF 2A MDRS; 8: LiF 1B MDRS, 9: SiC 1A MDRS. Segments between brackets mean that the lines measured on those different segments are consistent with the presented result, but was of lower quality and are therefore not included in the final results. The S/N level was averaged when more than one segment was used (though generally these ratios were similar in the different segments). (c) The stellar contribution ($\sim 30\%$; see text) was removed from these measurements.

(d) N I $\lambda 953.970$ is blended with N I $\lambda 954.104$ making these values uncertain.

(e) The stellar contribution ($\sim 7\%$; see text) was removed from these measurements, but N III $\lambda 989$ is also blended with Si II $\lambda 989.9$. This measurement supposes that the line is not saturated.

(f) This line is a triplet of lines blended at the *FUSE* resolution.

(g) Ar I $\lambda 1066.660$ is blended with the strong stellar Si IV feature at 1066.6 Å.

TABLE 2
D I MEASUREMENTS: AOD RESULTS

λ_{lab} Å	f	S/N	W_λ (mÅ)	$\log N_a$ (cm ⁻²)	Segment
1025.443	7.91×10^{-2}	35	34.2 ± 6.8	13.75 ± 0.09	LiF 1A MDRS
		35	$41.5 \pm 8.7^*$	$13.84 \pm 0.10^*$	LiF 1A MDRS
		27	32.9 ± 7.0	13.72 ± 0.10	LiF 2B MDRS
		44	37.5 ± 5.8	13.77 ± 0.08	LiF 1A LWRS
		26	40.4 ± 12.7	13.80 ± 0.15	LiF 2B LWRS
		23	39.3 ± 9.2	13.81 ± 0.16	SiC 1A LWRS
972.272	2.90×10^{-2}	20	11.5 : (< 14.8)	13.67 : (< 13.79)	SiC 1B LWRS
		20	13.2 : (< 14.8)	13.74 : (< 13.79)	SiC 1B MDRS
		23	18.9 :	13.92 :	SiC 2A LWRS
949.484	1.39×10^{-2}	27	10.8 : (< 11.3)	13.98 : (< 14.00)	SiC 1B LWRS

Note. — Uncertainties are 1σ error. Upper limits in brackets are 3σ estimates. Colons indicate that the value is uncertain. (See text for more details). (*) Stellar continuum, see text for more details.

TABLE 3
COLUMN DENSITIES WITH 2σ ERRORS

Ions	AOD	PF 1	PF 2	Adopted
D I	13.79 ± 0.14	$13.89 \pm \begin{smallmatrix} 0.05 \\ 0.06 \end{smallmatrix}$	13.86 ± 0.09	13.85 ± 0.09
C II*	13.06 ± 0.10	13.06 ± 0.10
N I	$14.33 \pm \begin{smallmatrix} 0.06 \\ 0.04 \end{smallmatrix}$	14.31 ± 0.04	14.37 ± 0.12	$14.34 \pm \begin{smallmatrix} 0.09 \\ 0.08 \end{smallmatrix}$
O I	$15.21 \pm \begin{smallmatrix} 0.10 \\ 0.08 \end{smallmatrix}$	$15.29 \pm \begin{smallmatrix} 0.06 \\ 0.05 \end{smallmatrix}$	15.27 ± 0.09	$15.26 \pm \begin{smallmatrix} 0.08 \\ 0.07 \end{smallmatrix}$
Ar I	12.86 ± 0.14	12.86 ± 0.14
Fe II	$12.88 \pm \begin{smallmatrix} 0.26 \\ 0.38 \end{smallmatrix}$	$13.00 \pm \begin{smallmatrix} 0.09 \\ 0.11 \end{smallmatrix}$...	$12.94 \pm \begin{smallmatrix} 0.23 \\ 0.31 \end{smallmatrix}$

Note. — AOD gives the results of the apparent optical depth method described in § 3.1. PF 1 and PF 2 refer to the two independent profile fitting analyses described in § 3.2.

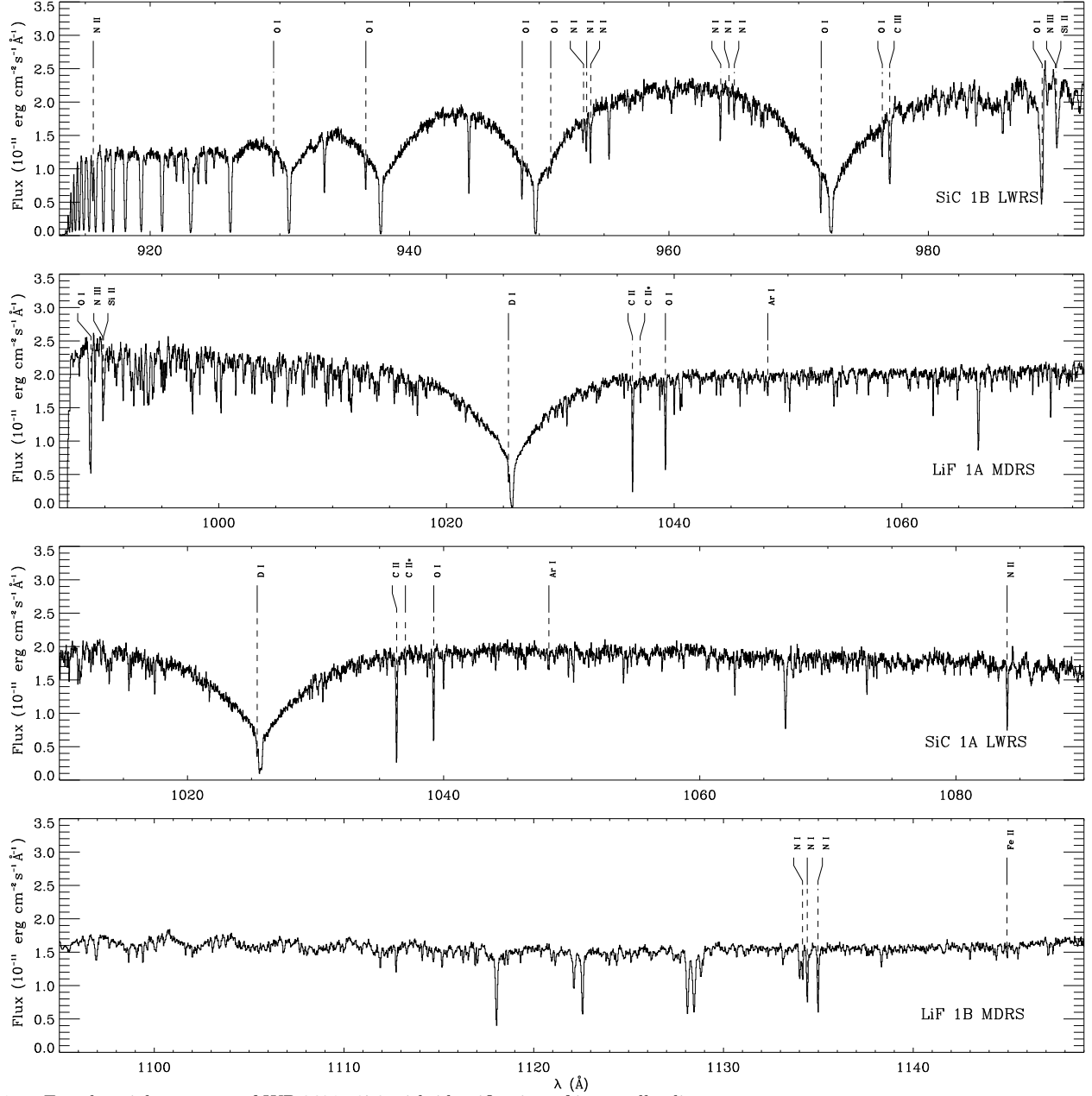


FIG. 1.— Far-ultraviolet spectra of WD 0621-376 with identification of interstellar lines.

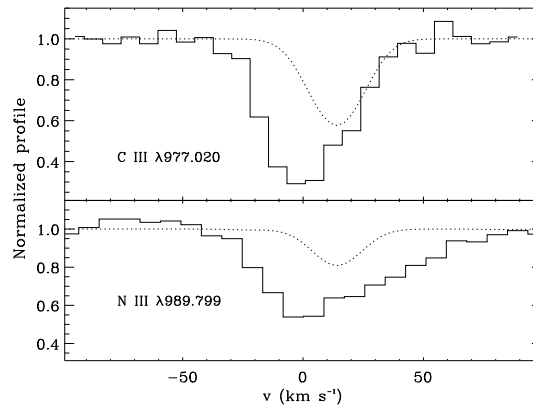


FIG. 2.— Spectra of C III and N III (histograms) and a model of stellar absorption (dotted lines). The N III feature shows clearly that interstellar Si II $\lambda 989.9$ must also be present.

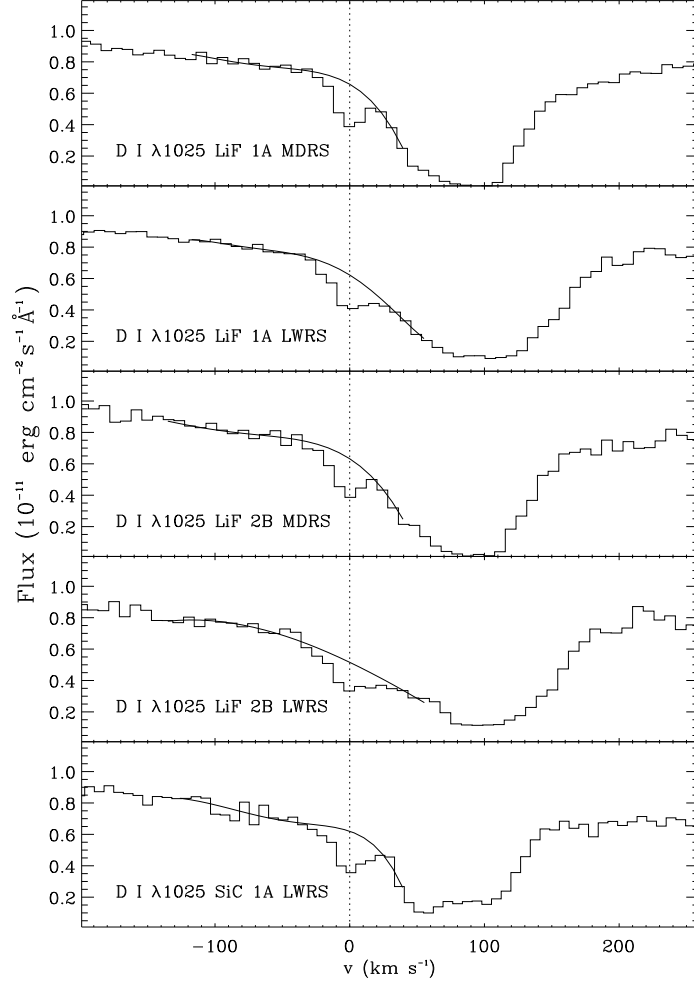


FIG. 3.— Spectra of D I Lyman- β in the different segments and local polynomial fits to the continua. Note how the shapes of the lines differ between segments in the LWRs data (even for essentially night data) because of the H I airglow, while for the MDRS the effect of airglow is smaller.

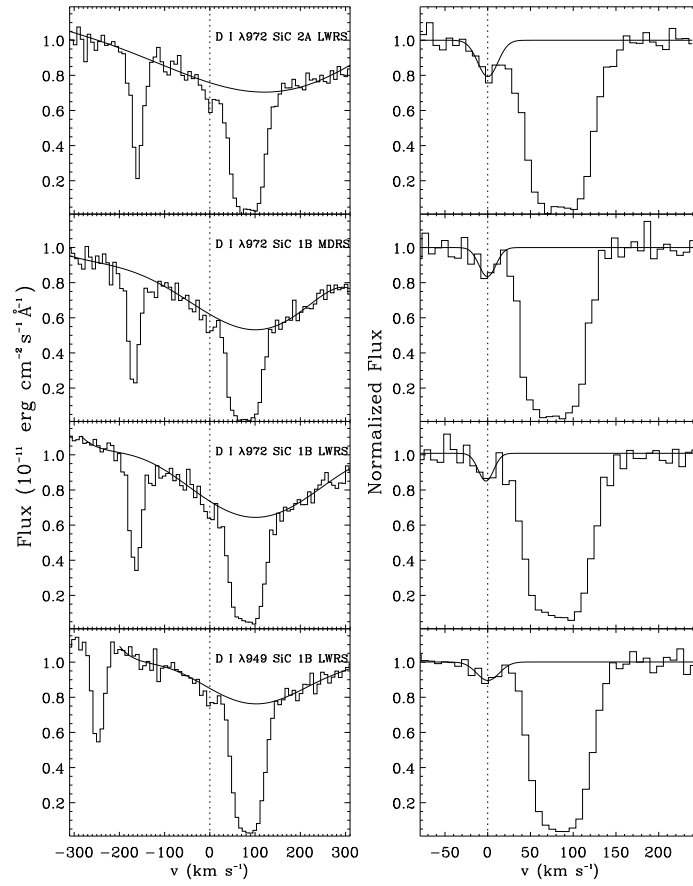


FIG. 4.— Detection ($2-3\sigma$) of the D I lines in the SiC channels. The left panel shows the calibrated flux in different segments (and wavelengths), while the right panel side presents their respective normalized profile with a gaussian fit.

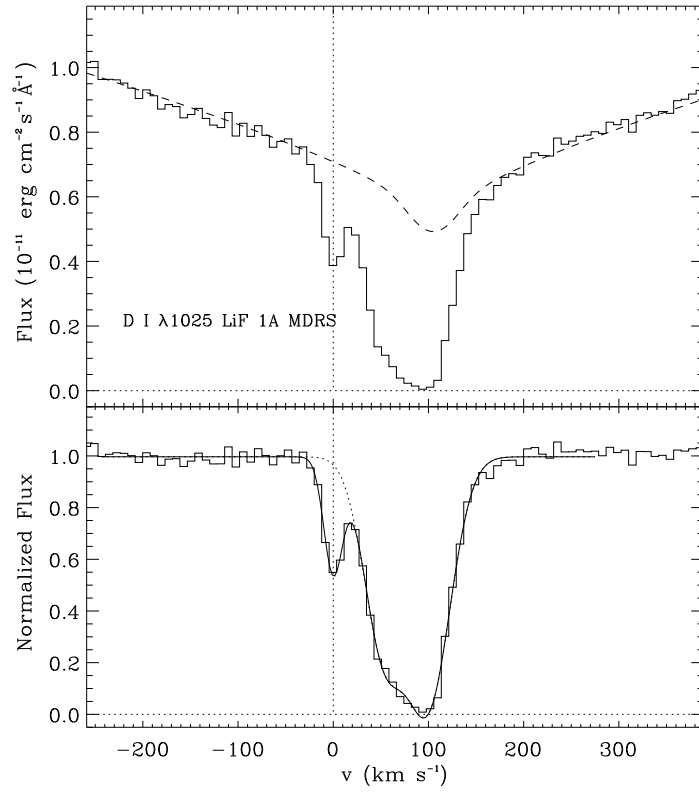


FIG. 5.— Spectrum of D I Lyman- β in the LiF 1A MDRS segment. Top panel: calibrated flux with the stellar continuum. Bottom panel: the resulting normalized profile with optimized gaussian fits (the solid line is the 3 gaussian component fit (D I and H I), while the dotted line is the 2 gaussian component fit (only H I); see text for more details).

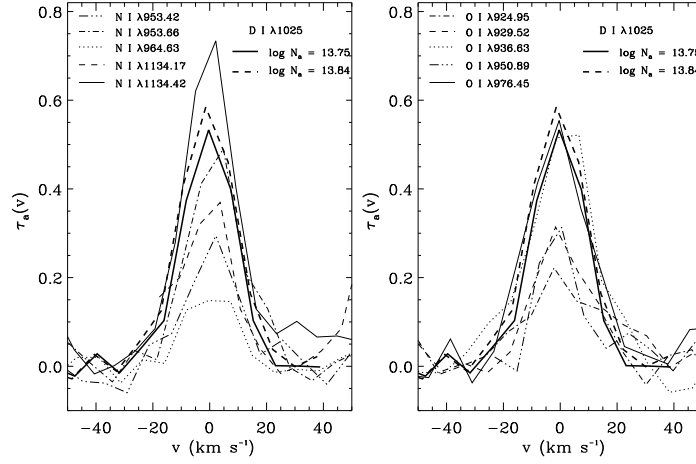


FIG. 6.— Apparent optical depths of D I Lyman- β for the two continuum placements (see § 3.1.2) compared to the unsaturated N I and O I.

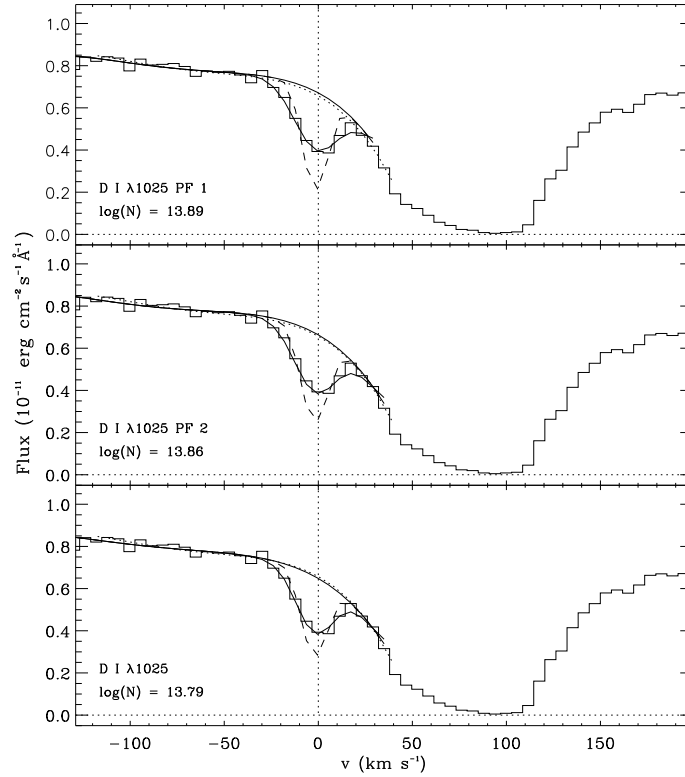


FIG. 7.— Spectrum of D I Lyman- β in the LiF 1A MDRS segment with fits from PF 1 and PF 2 (see § 3.2). The fitted profiles as well as the continua are drawn by a solid line while the dashed line shows the intrinsic profiles before convolution by the LSFs. The bottom panel shows the value derived with an Owens fit using the PF 2 method but with the D I column density set to the value (13.79 dex) derived from the AOD method. The dotted lines shown in the three panels indicate the continuum shown in the top panel of Figure 3.